

# Eye Tear Activated Mg-Air Battery Driven By Natural Eye Blinking For Smart Contact Lenses

**Erfan Pourshaban**

University of Utah

**Aishwaryadev Banerjee**

University of Utah <https://orcid.org/0000-0002-4092-7471>

**Mohit Karkhanis**

University of Utah

**Adwait Deshpande**

University of Utah

**Chayanjit Ghosh**

University of Utah

**Hanseup Kim**

University of Utah

**Carlos Mastrangelo** (✉ [carlos.mastrangelo@utah.edu](mailto:carlos.mastrangelo@utah.edu))

University of Utah

---

## Article

**Keywords:** Metal-Air Battery, Eye Blinking, Energy Generation, Smart Contact Lens

**Posted Date:** January 26th, 2022

**DOI:** <https://doi.org/10.21203/rs.3.rs-1172132/v1>

**License:**   This work is licensed under a Creative Commons Attribution 4.0 International License.

[Read Full License](#)

---

**Version of Record:** A version of this preprint was published at Advanced Materials Technologies on September 14th, 2022. See the published version at <https://doi.org/10.1002/admt.202200518>.

# Abstract

Smart, adaptive contact lenses (SCLs) are amongst the most anticipated, next-generation, standalone medical devices. SCLs require the integration of thin microelectronic components, tunable lenses, and micro-power sources onto a common non-planar substrate. Here, we report a miniaturized, sliding metal-air electrochemical micro-battery driven by natural eye blinking motion that can be integrated with an SCL platform as a source of electrical energy. The metal-air battery ( $3.8 \text{ mm}^2$ ) consists of a Mg anode and a Pt cathode. The electrolyte of the battery is the eye-tear liquid and is introduced to the battery structure during the natural eye-blinking cycle, which activates the battery. The open-circuit voltage across the eye-tear activated metal-air battery (ETMAB) was measured to be 2.2 V and the maximum specific capacity of  $3561 \text{ mA h g}^{-1}$  was obtained at a discharge current density of  $5 \text{ mA}\cdot\text{cm}^{-2}$ . Impedance matching analysis exhibits the maximum generated power density of  $1.3 \text{ mW}\cdot\text{cm}^{-2}$  at the load of  $740 \Omega$ .

## 1. Introduction

An ever-growing demand for smart health care has led to the development of smart contact lenses (SCLs). Currently, the proposed applications of SCLs include vision correction<sup>1</sup>, augmented/virtual reality (AR/VR)<sup>2</sup>, drug delivery<sup>3</sup>, glucose detection, and disease diagnosis<sup>4</sup>. SCLs for vision correction typically comprise of an autofocusing tunable lens<sup>5</sup>, eye-tracking system<sup>6</sup>, communication antennas<sup>7</sup> and integrated electronic sub-systems, which require a reliable source of electrical power for operation. The lack of an appropriate low-profile energy source which can be integrated with SCLs is a major obstacle to development and practical realization. Power-generation techniques such as photovoltaics<sup>8,9</sup>, wireless power transfer<sup>10</sup>, and conventional batteries<sup>11</sup> have been utilized for reliable power of wearables, but they suffer from several drawbacks with SCLs. For example, solar cells require a continuous light source and provide low power under low-intensity indoor lighting conditions<sup>9</sup>. Wireless power-transfer schemes require receiver and transmitter antennas that typically limit the transfer distance ( $<10 \text{ cm}$ )<sup>12</sup> and require additional external components. Rechargeable Li-ion batteries are constructed with bio-hazardous materials and require significant packaging and footprint/thickness. Therefore, it is imperative to develop new energy-generation and storage schemes that are biocompatible, energy-efficient, and suitable for integration with standalone SCLs.

An alternative high energy density power source is a metal-air (MAB) battery. A typical MAB comprises of a metal anode, an air-breathing cathode, and an electrolyte. Theoretically, certain MABs<sup>13</sup> have demonstrated a much greater specific capacity and energy-density than typical lithium-ion batteries, but technical challenges such as parasitic corrosion of anode material and continuous requirement of oxygen have hindered their commercial implementation<sup>14</sup> and restricted their use to low-power applications such as miniature hearing aids<sup>15,16</sup>. However, if the MAB could be operated under conditions of continuous electrolyte replenishment, unlimited supply of  $\text{O}_2$ , and suppression of electrochemical polarization, one can significantly extend the lifetime of such batteries while delivering high power-output.

This is precisely what is achieved when the MAB is driven using natural eye-blinking and the electrolyte (eye-tear liquid) is periodically replenished.

In this paper, we demonstrate a highly novel power-generation scheme that utilizes the natural eye-blinking motion to regenerate a bio-compatible metal-air battery. The MAB is independent of any external energy-sources, can be easily integrated with an SCL system, and it can reliably deliver electrical power to SCL components over extended periods of time. Specifically, this article describes the eye tear MAB (ETMAB) working-principle, device structure and fabrication, and characterization of the MAB performance. The paper also explores different metals as suitable candidates for cathode/anode material to optimize the device output. The motion-activated Mg-air battery demonstrates a cumulative energy density of  $8.3 \text{ J}\cdot\text{cm}^{-2}$ . Experiments exhibit the maximum voltage and current output of 2.2 V and 1.48 mA, The energy density is greater than that achieved with Li-based micro-batteries for IoT applications<sup>17-19</sup> and previously reported biofluid-activated Mg-based batteries<sup>20-22</sup>.

## 2. Methods And Materials

### 2.1. Device Structure and Fabrication

The micro-fabricated metal-air battery (MAB) essentially consists of an anode and a cathode electrode material, deposited on a thermally oxidized silicon chip ( $500 \mu\text{m}$ ). Supplementary Fig. S1 shows the schematic of the device structure and the simplified fabrication flow. The different metals studied as candidates for anode material were Cu, Al, Mg, Fe and Zn. Pt, Au, Co and Ni were investigated as cathode candidates. Cu ( $200 \text{ nm}$ ), Al ( $200\text{nm}$ ), Ni ( $200\text{nm}$ ), Co ( $200\text{nm}$ ), Au ( $200\text{nm}$ ), and Pt ( $200\text{nm}$ ) were deposited on thoroughly cleaned silicon chip using the sputtering technique in the Denton Discovery 18 magnetron sputtering system. A thin adhesion layer of Cr ( $20 \text{ nm}$ ) was also sputter deposited on the silicon chip prior to the deposition of the cathode material. For the remaining anode candidates, commercially available Mg foil (purity 99.95% with the thickness of  $200 \mu\text{m}$ ), Fe foil (purity of 99.995% with the thickness of  $100 \mu\text{m}$ ), and Zn foil (purity 99.999% with the thickness of  $80 \mu\text{m}$ ) were utilized. Cytop (CTL-800M) was spin-coated at 3000 rpm for 60s on the device and heated at  $200^\circ\text{C}$  in an atmospheric Memmert oven to realize a  $1 \mu\text{m}$  thick hydrophobic coating, which was partially dry-etched with RIE technique (using plasma of  $\text{CF}_4/\text{O}_2$ ) to expose the metal contacts. The presence of the hydrophobic fluorinated material (Cytop) helps in efficient de-wetting of the anode/cathode surface after each cycle of an eye blinking motion, which removes any internal parasitic charge flow and enhances the lifetime of the device. Finally, a commercially available moisturizing eye drop (Refresh Plus Lubricant Eye Drops containing 0.5% Carboxymethylcellulose Sodium as an eye lubricant) was used to replicate the human eye tear, which acted as the electrolyte for the battery. According to the American Academy of Optometry, the pH of this moisturizing eye drop is the same as natural tears' pH<sup>23</sup>. It is important to note that although the proof of principle has been demonstrated using  $500 \mu\text{m}$  thick silicon chip, the MAB can also be built on much thinner and flexible substrates for integration with SCLs. Section 2.2 describes the fabrication of the MAB on a flexible, polyimide (PI) substrate.

## 2.2. Experimental Methods

The natural eye-blinking motion recurrently irrigates the surface of the eye using eye-tear fluid and lubricant oil (produced by the Meibomian glands<sup>24-26</sup>) thus refreshing the fluid in contact with the electrodes. As a result of the eyelid motion, the electrodes essentially remain under one of three conditions: (a) fully covered by the eye-tear fluid (completely shut eyelid), (b) partially covered by the eye-tear (during the cycle of an eye-blink) or (c) not in contact with the eye-tear (when the eyelid is completely open).

*Dynamic Linear Slide Mode:* We simulated these repetitive conditions using a microcontroller driven linear servo actuator (Firgelli\_FA-RA-22-12-2), which provided a periodic relative motion between the metal (anode/cathode) deposited silicon chip and the moisturizing eye-drop (100  $\mu$ l), as shown in Fig. 1. This experiment is henceforth referred to as the dynamic mode of operation. The electrolytic solution was replenished every 100 cycles to replicate the natural eye-blinking condition.

*Static Mode:* In order to investigate the specific effect of the eye-blinking motion, we also characterized the MAB performance under static, zero flow condition with the electrodes in contact with the eye-drop and we compared it to the performance observed under the dynamic mode. As shown in Fig. S2, for the static test setup, a stagnant fluid cavity polydimethylsiloxane (PDMS, Sylgard 184, Dow Corning) enclosure was fabricated on top of the electrodes by pouring PDMS mixture (1:10, curing agent: base polymer) into a rectangular mold (3.8 mm<sup>2</sup>) and curing it at 100°C for 1 hr. The cured PDMS (1 mm thick) with the rectangular cavity was next peeled off from the mold and plasma-bonded to the device's substrate. The moisturizing eye drop was then carefully injected into the cavity to ensure that it properly covers the anode and cathode. The injection inlet was sealed with a PI film.

*Dynamic Angular Mode:* Finally, to more closely replicate the angular motion of the human eyelid, we attached a 3D printed eyelid model to a brushless servo motor (SAVOX SB-2272MG) capable of providing angular motion. Similar to the deposition processes shown in Section 2.1, the metal electrodes were sputter deposited on a flexible polyimide (PI) tape, which was attached to a parylene coated (3  $\mu$ m thick) glass slide. The PI tape was then easily peeled off and then attached to the eyelid replica. As shown in Fig. S3, the servo motor provides the relative angular motion between the 3D printed eye-lid and the eye-drop.

## 2.3. Characterization Techniques

All voltage measurements were made by probing the electrodes of the battery using a digital oscilloscope (Siglent SDS1202X-E) with the input impedance of 1 M $\Omega$  and the input capacitance of 15 pF. A Tencor P-10 profilometer was used to measure the thickness of the electrodes and the Cytop. X-ray diffraction (XRD, Rigaku Ultima IV diffractometer with Cu K $\alpha$  radiation,  $\lambda = 1.5418 \text{ \AA}$ ) measurements were conducted at the scan rate of 0.02°/step to analyze the structural properties of the Mg anode before and after the electrochemical reactions occurring during battery operation. To precisely detect the surface structure of the Mg anode after the electrochemical reactions, we performed grazing incident XRD ( $2\theta = 1^\circ$ ). High-

resolution imaging was performed using scanning electron microscopy (SEM, FEI Quanta 600F) together with energy dispersive spectroscopy (EDS) to investigate the morphological and elemental features of the Mg anode, before and after battery usage. The short circuit current output of the device was measured using a Stanford Research Systems (SR570) low noise preamplifier with the DC input impedance of  $1\Omega$  for a sensitivity of  $500\ \mu\text{A}\cdot\text{V}^{-1}$ . In order to investigate the maximum power output of different electrochemical cells, impedance matching analysis was carried out using different resistive loads including 0.08, 0.12, 0.74, 4, 12, 56, 90 k $\Omega$ . A Hewlett-Packard precision parameter analyzer 4145A was used to measure the internal impedance of the device. A Gamry Potentiostat Reference 600 was utilized to measure the potential response and the cyclic-voltammetry analysis from -1 to 1 V (Ag/AgCl (Sat.) as the reference electrode) with the scan rate of 50 mV/s to characterize the electrochemical performance of the MAB. In order to elucidate the physical mechanism behind our device and observe the effect of oxygen on its electrochemical performance, we introduced oxygen to the electrolytic solution using a compressed  $\text{O}_2$  gas cylinder. An Agilent 8900 ICP-QQQ tandem quadrupole mass-spectrometer and 945 professional conductivity detector from Metrohm were used to detect the concentration of Mg ions in the eye-tear solution and its conductivity in different time periods, respectively.

### 3. Results And Discussion

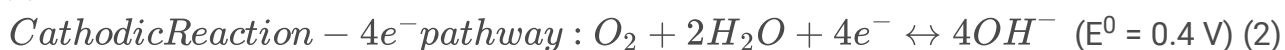
#### 3.1. ETMAB Working Principle and Design Considerations

As described in Section 2.2 and illustrated in Fig. 1, the dynamic mode of operation involves a linear actuator that provides relative motion between the liquid eye-drop (electrolyte) and the cathode/anode metals that are present on the surface of the device structure. First, the eye-drop is not in contact with any of the polarizable electrodes, and the battery is not activated (off-mode). Next, due to the actuator's linear motion, the liquid gradually covers the device's surface. When the liquid comes in contact with the anode-metal, spontaneous electrochemical anodic reactions are initiated which generate electric charges. Finally, when the eye-drop comes in contact with both the anode and the cathode, the battery is activated (on-mode) and the generated electrons can be used to deliver electric power to an external load.

The fundamental working principle of the ETMAB is the eye-blinking driven generation of free electrons which are a product of anodic electrochemical reactions and subsequent electron-transfer to an external load, along with the oxygen reduction reactions (ORRs) on the air-breathing cathode (air-electrode) that occur when the eye-tear comes in contact with the ETMAB. The generalized redox reactions at the anode and cathode for a typical MAB are:



(1)





Therefore, correct selection of anode and cathode materials is critical to optimize the performance of the ETMAB. The first half-reaction (1) involves the oxidation of the anode material. Therefore, candidates for the anode were selected based on their standard electrode potentials. Although lithium (Li) has been extensively utilized as an anode material for metal-air and metal-ion batteries<sup>27-29</sup>, it is biohazardous and is therefore extremely unsuitable for integration with SCL. Furthermore, Li suffers from calcination induced dendrite formation that severely limits the efficiency of Li-air batteries, and such systems typically require an intercalation compound for proper functioning<sup>30</sup>. Therefore, alternative anode-materials might provide substantial advantages over Li. For example, Mg-anode does not suffer from dendritic formation, is earth-abundant ( $10^4$  times compared to Li)<sup>31</sup>, ecofriendly<sup>32</sup>, and a biocompatible element<sup>33</sup>. Furthermore, the Mg-air battery has a greater theoretical specific energy density ( $3.9 \text{ kW h kg}^{-1}$ ) than the Li-air ( $3.4 \text{ kW h kg}^{-1}$ ) counterpart<sup>34-36</sup>. An in-depth analysis of different anode materials has been provided in section 3.3.

The other half-reaction involves the reduction of oxygen at the air-cathode, which is the performance limiting electrode in metal-air batteries due to the sluggish nature of ORR reactions<sup>37</sup>. As shown in the reactions (2-4), the oxygen reduction reactions can take place through two different pathways known as 4 electrons (direct) or series of 2 electrons (indirect) pathway<sup>38,39</sup>. The formation of  $HO_2^-$  is the oxygen reduction rate limiting factor. At the cathode site, the electrode material is in contact with both the dissolved oxygen within the electrolyte (in our case the eye tear fluid) and the ambient gaseous oxygen. Therefore, the ORRs take place at triple-phase boundary, which is also commonly observed in solid-oxide fuel cells<sup>40</sup>. Hence, it is important to properly design the cathode architecture to ensure a maximum triple-phase boundary. Furthermore, the adsorption/desorption kinetics of the dissolved and ambient oxygen, is a fundamental property of the cathode material, and strongly affects the performance of ETMAB. Therefore, careful selection of cathode material is key to realizing an optimized output. Accordingly, different materials have been investigated as potential candidates for air-breathing cathodes, the details of which are provided in section 3.2.

Finally, according to the Nernst equation, for a given standard electrode potential and temperature, the reduction potential of a metal-air battery is directly proportional to the activities or effective concentration of oxygen accessible by the cathode<sup>41</sup>.

$$\text{Nernst Equation} : E_{Cell} = E_0 + 2.3026 \frac{RT}{nF} \log \frac{[Ox]}{[Red]}$$

(5)

Where,  $E_0$  is the standard potential,  $R$  is the universal gas constant,  $n$  is the number of transferred electrons,  $F$  is Faraday's constant,  $T$  is the temperature,  $[Ox]$  and  $[Red]$  are the activities of the oxidant and reductant elements. The availability of oxygen in the ETMAB strongly affects the battery output. This is a significant bottleneck that has restricted widespread usage of MABs and it typically requires

sophisticated ORR catalyst materials or periodic replenishment of electrolytes<sup>42,43</sup>. The advantage of utilizing naturally available eye tear as the electrolyte for the ETMAB is that proper body functions ensure stable and continuous supply of dissolved oxygen to the eye tear fluid without the need of external provisions<sup>44</sup>. Furthermore, the placement of the SCL on the eye also ensures near-unlimited supply of gaseous oxygen from the atmosphere. Herein lies the greatest advantage of our ETMAB technology. The following sections provide in-depth analysis and characterization of the various components of the ETMAB.

## 3.2. Air Cathode Electrode Selection and Characterization

Figure 2 (a-c) show the open-circuit voltage, maximum short-circuit current output, and impedance-matched power-density of ETMABs featuring different air cathode electrode materials (Pt, Au, Co, and Ni) and Al as the anode material. The instantaneous current spikes are the result to the sudden contact of the electrolytic solution with the edge of the cathode. The ETMAB with Al anode and Pt cathode produced a highest open-circuit voltage of 1 V and a maximum short circuit current of 110  $\mu\text{A}$ . It produces the highest power density of  $70 \mu\text{W}\cdot\text{cm}^{-2}$  while driving a load of 12  $\text{k}\Omega$ .

The Al-air ETMAB using Pt as the air-electrode is able to charge a 100  $\mu\text{F}$  capacitor in 13 s, corresponding to an average power density of  $14.5 \mu\text{W}\cdot\text{cm}^{-2}$  (Fig. 2f). Integration of the current vs. time curve over one pulse (blink) demonstrates a total generated charge of 103.4  $\mu\text{C}$ . Therefore, the eye tear-activated Al-air battery with Pt cathode generates a maximum energy of 103.4  $\mu\text{J}$  per blinking cycle. The detailed voltage and current outputs of ETMABs with other metal cathodes is shown in supplementary Fig. S4 and Table. S1.

We believe the observed electrical output differences are explained by differences in the electrode oxygen reduction reactions (ORR) kinetics. Our data is consistent with that from other reports indicating the ORR kinetics of Pt is highest amongst metals<sup>38</sup>. Previous studies demonstrate that the ORR on the surface of the Pt predominantly undergoes the  $4\text{e}^-$  pathway<sup>45</sup> while a series of  $2\text{e}^-$  pathways occur for gold and the transition metal cathodes<sup>46,47</sup>. Additionally, as shown in Fig. 2g, cyclic voltammetry (CV) measurements performed on different cathode materials demonstrated the maximum current density for Pt with the current magnitude of  $760 \mu\text{A}\cdot\text{cm}^{-2}$  at ORR's potential (-0.2 V with respect to the Ag/AgCl reference electrode). This is a direct measure of comparative ORR kinetics also in agreement with previous studies. Detailed CV plots for each of the cathode materials are provided in the supplementary information, Fig. S5.

Figure 2i shows the load line and impedance matching power output plots of the Al-air ETMAB using Pt as the air-electrode (detailed plots for Al-air ETMAB using the other cathode materials are shown in supplementary information Fig. S6). Due to the highest power-density output, Pt was selected as the cathode material for further experiments.

## 3.3. Selection and Characterization of Anodes

Using Pt as the cathode material, several metals including Cu, Fe, Zn, and Mg were explored as potential candidates for the anode material. Fig. 3 (a-c) show the open-circuit voltage, maximum short-circuit current output, and impedance-matched power-density of Pt cathode based ETMABs featuring different anode materials.

The plots summarized in Table. S2 indicate the highest open-circuit voltage, maximum short circuit current and power-density outputs were measured when using Mg as the anode. The results agree with the electro-chemical series since the electrode potential of Mg (w.r.t a standard hydrogen electrode) is lower than that of the other anode material candidates. As shown in Fig. 3 (d-f), the open-circuit voltage and short-circuit current output were measured to be 2.2 V and 1.48 mA respectively. These values closely follow the redox reactions and the electrode potentials of the anode materials (see supplementary information for the electrochemical reactions of Mg-air ETMAB).

The integration of the current vs. time curve over one pulse for the Mg-air ETMAB represents charge generation of 2.8 mC, corresponding to a generated energy of 6.1 mJ per blink cycle. The maximum power-density was measured to be  $1.3 \text{ mW}\cdot\text{cm}^{-2}$  at the discharge current density of  $3 \text{ mA}\cdot\text{cm}^{-2}$  while driving an external resistive load of  $740 \Omega$ , which corresponds to the internal resistance of the Mg-air ETMAB. This battery exhibited a maximum specific capacity of  $3561 \text{ mA h g}^{-1}$ , which is much greater than commonly used 3D micro-batteries ( $\sim 220 \text{ mA h g}^{-1}$ ) for IoT applications<sup>17-19</sup>. Detailed electrical information of the other anodes is shown in supplementary Fig. S7 and Table. S2. Experimental results clearly indicate that amongst the various ETMAB configurations investigated, the Mg-air ETMAB (with the Pt cathode) demonstrated the highest output and was therefore selected for further characterization and analysis.

### 3.4. Mg-air ETMAB's Practical Applications

Figure 4a exhibits the load line and impedance matching power output of the Mg-air ETMAB, which is very useful to choose correct electrical circuits for the practical applications (detailed information and plots for the Pt cathode based ETMAB using other anode materials are shown in the supplementary Fig. S8). The Mg-air ETMAB was utilized to completely charge-up a commercially available 11 mF chip type electric double layer super-capacitor in 5 min (Fig. c and d). Interestingly, unlike the Mg-air ETMAB, which takes approximately 11 hr to completely discharge under continuous, non-stop frequent motion, the commercial super-capacitor immediately discharges under the same loading condition. Additionally, four commercially available red LEDs ( $V_F = 1.6 \text{ V}$  and Current-Test = 1 mA) were switched on using the Mg-air ETMAB (Fig. 4b and supplementary video 1), thereby demonstrating the practical viability of our developed air-battery.

As shown previously in Fig. 4 (e) and (f), since the voltage and current outputs of our ETMAB are pulsed, it is important to first convert the time-varying output to a stable DC level so that the battery can be used to supply power to commonly used microelectronic ICs, which typically require DC voltage to function properly. In order to do so, we designed and implemented a voltage multiplier circuit (Dickson

configuration<sup>48</sup>) that consists of 5 electrolytic capacitors (4.7  $\mu\text{F}$ ) and 5 Schottky diodes (1N4148), to convert the AC output of the Mg-air ETMAB to DC output and boost the voltage to 3.3 V. Fig. 4e shows the circuit diagram and Fig. 4f shows the output of the voltage-multiplier circuit.

### 3.5. Comparison of Static vs. Dynamic Mode of Operation of Mg-air ETMAB

Fig. 5 (a-e) show the open-circuit voltage, current, load-line, impedance matching power output, and cumulative energy density of the Mg-air ETMAB operated under static and dynamic mode of operation.

Figure 5 (c) shows the cumulative energy density output of  $\sim 8 \text{ J}\cdot\text{cm}^{-2}$  for the motion-activated Mg-air ETMAB under the maximum power point at a load of  $740 \Omega$ , corresponding to the discharge current density of  $3 \text{ mA}\cdot\text{cm}^{-2}$ . This cumulative energy output is more than 8 times greater than that of the static Mg-air battery and therefore clearly indicates that the performance of the Mg-air ETMAB operated under the dynamic conditions is significantly greater than that of the static condition. Furthermore, the dynamic mode of operation exhibits the lifetime of 550 hr, which is more than 10 times longer than that of the static counterpart. We believe this is mainly due to three reasons. First, the eye tear is continuously replenished every single time an eye-blinking cycle occurs thereby providing a stable and abundant supply of dissolved oxygen to the ETMAB. This also ensures the stable value of the electrolyte resistance. ICP-MS together with the liquid conductivity measurement were conducted to analyze the effect of Mg dissolution on the electrolyte resistance (See supplementary Fig. S9). Second, since the ETMAB is an open electrochemical cell, it has access to near-unlimited ambient oxygen. These conditions, which are realized during the dynamic mode of operation, ensure continuous supply of oxygen to the ETMAB, which is crucial for proper functioning of the battery. Third, the repetitive back and forth motion in the dynamic mode helps to reduce the parasitic formation of effervescent cloud on the anode during the electrochemical reactions. On the contrary, in the static mode as the dissolution of the anode progresses, the stagnant electrolyte's resistance decreases, resulting in an increasing internal current flow which reduces the battery life and output energy.

In order to confirm the importance of oxygen availability in the ETMAB's performance, we also performed a series of CV tests while changing the oxygen level in the electrolytic solution by placing a microtube into the testing electrolyte to introduce  $\text{O}_2$  gas. Fig. 5 (f) demonstrates the CV results of the Mg-air battery while testing under different atmospheric conditions. The current density at the oxygen reduction potential varies by introducing more oxygen to the media. An  $\text{O}_2$ -rich media provides higher current density. This proves that an  $\text{O}_2$ -rich media provides higher current density, thereby demonstrating the importance of oxygen availability in the electrochemical performance of the Mg-air battery.

We also investigated the cause of the finite life of Mg-air ETMAB. A series of XRD measurements were conducted both on the Mg anode and Pt cathode before and after operating the battery for some time. Supplementary Fig. S10 shows no detectable change in the structural properties of the Pt cathode after 40000 s of the dynamic mode of operation. Therefore, it follows that the battery termination mechanism

stems from the anode's surface passivation. The XRD spectrum of the anode (JCPDS card No. 44-1482) clearly shows traces of magnesium hydroxide with Brucite structure formed on the surface of the Mg anode (Supplementary Fig. S10). We believe the hydroxide layer inhibits further oxidation reactions on the Mg anode. To further characterize the morphological and structural properties of the anode's surface after the extended (40000 s) frequent sliding motion, we also carried out EDS analysis at the accelerating voltage of 5 KV. Fig. 6 exhibits the formation of the urchin-like magnesium hydroxide on the surface of the Mg anode after the electrochemical reactions. Fig. S11 also exhibits the cross-section SEM images showing the formation of the magnesium hydroxide on the surface of the Mg anode.

### 3.6. Mg-air ETMAB as a Power Source for Smart Contact Lenses

The greatly improved performance of the Mg-air ETMAB compared to static, motionless MAB battery makes the ETMAB suitable for powering autonomous systems that undergo periodic motion. We utilized the ETMAB to power a smart contact lens (SCL) employing natural eye-blinking motion. Eye blinking is a natural muscle movement that occurs over  $10^4$  times a day<sup>49,50</sup>. Fig. 7 schematically illustrates the working mechanism with two different blinking conditions, including, non-stop continuous blinking motion (b, c) and blinking every 5 s (d, e). When the eye is open, the device is in the off-mode. When the eye is closing, it goes into contact with the anode material. Thus, the electrochemical reactions and the charge generation begin. Finally, the power generation starts when the eyelid touches the air-electrode, and the device goes in the on-mode. The frequent natural eye-blinking generates electrical power which can be used to drive electronic components on the SCL. To demonstrate the feasibility of the concept we performed additional open-circuit voltage and short-circuit current measurements while conducting angular sweeps. A Mg-air ETMAB mounted on 3D printed eyeball replica fully charges up a 100  $\mu\text{F}$  capacitor after 4 blinking cycles with a speed of  $15 \text{ cm}\cdot\text{s}^{-1}$  and a blinking frequency of 12 times per min (200 mHz), which is an average blinking frequency of an adult<sup>49</sup> (See the supplementary video 2).

## 4. Conclusions

We introduced a new moving fluid metal air battery suitable for providing power to smart contact lenses driven by natural eye blinking. We have conducted a series of electrical and electrochemical experiments to explore the best battery electrode material selection. The Mg-air battery using Pt as the air-electrode and moisturizing eye drop as the electrolyte shows the most energy output. The battery open-circuit voltage of 2.2 V and the short circuit current density of  $6 \text{ mA}\cdot\text{cm}^{-2}$  were achieved. Remarkably, the motion-activated mode with a specific capacity of  $3561 \text{ mA h g}^{-1}$  is much more powerful than the encapsulated and stationary Mg-air cell. Furthermore, the tear-activated mode provides a cumulative energy density of  $\sim 8 \text{ J}\cdot\text{cm}^{-2}$ , which is 8 times higher than that achievable in motionless static mode.

## References

1. Vásquez Quintero, A., Pérez-Merino, P. & De Smet, H. Artificial iris performance for smart contact lens vision correction applications. *Sci. Rep.* **10**, 14641 (2020).
2. Jones, L. *et al.* BCLA CLEAR – Contact lens technologies of the future. *Contact Lens Anterior Eye* **44**, 398–430 (2021).
3. Keum, D. H. *et al.* Wireless smart contact lens for diabetic diagnosis and therapy. *Sci. Adv.* **6**, eaba3252 (2020).
4. Kusama, S., Sato, K., Yoshida, S. & Nishizawa, M. Self-Moisturizing Smart Contact Lens Employing Electroosmosis. *Adv. Mater. Technol.* **5**, 1900889 (2020).
5. Banerjee, A. *et al.* Low-power, thin and flexible, stacked digital LC lens for adaptive contact lens system with enhanced tunability. in *Conference on Lasers and Electro-Optics (2021)*, paper AF2Q.8 AF2Q.8 (Optical Society of America, 2021). doi:10.1364/CLEO\_AT.2021.AF2Q.8.
6. Ghosh, C. *et al.* Low-Profile Induced-Voltage Distance Ranger for Smart Contact Lenses. *IEEE Trans. Biomed. Eng.* **68**, 2203–2210 (2021).
7. Park, J. *et al.* Soft, smart contact lenses with integrations of wireless circuits, glucose sensors, and displays. *Sci. Adv.* **4**, eaap9841 (2018).
8. Pourshaban, E. *et al.* Semi-transparent and Flexible Single Crystalline Silicon Solar Cell. in *IEEE Journal or photovoltaics* (IEEE Journal or photovoltaics).
9. Pourshaban, E. *et al.* Micromachined Flexible Semi-Transparent Silicon Solar Cells as Power Sources for Microsystems. in *2021 IEEE 34th International Conference on Micro Electro Mechanical Systems (MEMS)* 246–249 (2021). doi:10.1109/MEMS51782.2021.9375382.
10. Pandey, J. *et al.* A Fully Integrated RF-Powered Contact Lens With a Single Element Display. *IEEE Trans. Biomed. Circuits Syst.* **4**, 454–461 (2010).
11. Nasreldin, M. *et al.* Flexible Micro-Battery for Powering Smart Contact Lens. *Sensors* **19**, 2062 (2019).
12. Takamatsu, T., Chen, Y., Yoshimasu, T., Nishizawa, M. & Miyake, T. Highly Efficient, Flexible Wireless-Powered Circuit Printed on a Moist, Soft Contact Lens. *Adv. Mater. Technol.* **4**, 1800671 (2019).
13. Wang, H.-F. & Xu, Q. Materials Design for Rechargeable Metal-Air Batteries. *Matter* **1**, 565–595 (2019).
14. Li, Y. & Lu, J. Metal–Air Batteries: Will They Be the Future Electrochemical Energy Storage Device of Choice? [Metal-Air Batteries: Future Electrochemical Energy Storage of Choice?]. *ACS Energy Lett.* **2**, (2017).

15. Sparkes, C. & Lacey, N. K. A study of mercuric oxide and zinc-air battery life in hearing aids. *J. Laryngol. Otol.* **111**, 814–819 (1997).
16. Hussain, M. A., Gharghan, S. K. & Hamood, H. Q. Design and Implementation of Wireless Low-Power Transfer for Medical Implant Devices. *IOP Conf. Ser. Mater. Sci. Eng.* **745**, 012087 (2020).
17. Wang, C. *et al.* Carbon-MEMS architectures for 3D microbatteries. in *MEMS, MOEMS, and Micromachining* vol. 5455 295–302 (SPIE, 2004).
18. Dunn, B., Kim, C.-J. & Tolbert, S. Three-dimensional microbatteries for MEMS/NEMS technology. in *2010 IEEE 23rd International Conference on Micro Electro Mechanical Systems (MEMS)* 164–167 (2010). doi:10.1109/MEMSYS.2010.5442541.
19. Toor, A. *et al.* Stencil-printed Lithium-ion micro batteries for IoT applications. *Nano Energy* **82**, 105666 (2021).
20. Lee, K. B. Urine-activated paper batteries for biosystems. *J. Micromech. Microeng.* **15**, S210–S214 (2005).
21. Ortega Tana, L., Llorella, A., Esquivel, J. P. & Sabate, N. Self-powered smart patch for sweat conductivity monitoring. in *Smart Systems Integration; 13th International Conference and Exhibition on Integration Issues of Miniaturized Systems* 1–3 (2019).
22. Liu, G. *et al.* A wearable conductivity sensor for wireless real-time sweat monitoring. *Sens. Actuators B Chem.* **227**, 35–42 (2016).
23. Carney, L. G., Mauger, T. F. & Hill, R. M. Buffering in human tears: pH responses to acid and base challenge. *Invest. Ophthalmol. Vis. Sci.* **30**, 747–754 (1989).
24. Knop, N. & Knop, E. [Meibomian glands. Part I: anatomy, embryology and histology of the Meibomian glands]. *Ophthalmol.* **106**, 872–883 (2009).
25. Singh, S., Naidu, G. C., Vemuganti, G. & Basu, S. Morphological variants of meibomian glands: correlation of meibography features with histopathology findings. *Br. J. Ophthalmol.* (2021) doi:10.1136/bjophthalmol-2021-318876.
26. Kiyat, P., Palamar, M., Gerceker Turk, B. & Yagci, A. Dry Eye and Quantitative and Qualitative Changes of Meibomian Glands in Patients With Pemphigus. *Cornea* **39**, 1108–1111 (2020).
27. Liu, Q.-C., Xu, J.-J., Xu, D. & Zhang, X.-B. Flexible lithium–oxygen battery based on a recoverable cathode. *Nat. Commun.* **6**, 7892 (2015).
28. Jung, H.-G., Hassoun, J., Park, J.-B., Sun, Y.-K. & Scrosati, B. An improved high-performance lithium–air battery. *Nat. Chem.* **4**, 579–585 (2012).

29. Moeremans, B. *et al.* Lithium-ion battery electrolyte mobility at nano-confined graphene interfaces. *Nat. Commun.* **7**, 12693 (2016).
30. Van der Ven, A., Bhattacharya, J. & Belak, A. A. Understanding Li Diffusion in Li-Intercalation Compounds. *Acc. Chem. Res.* **46**, 1216–1225 (2013).
31. Liu, F., Wang, T., Liu, X. & Fan, L.-Z. Challenges and Recent Progress on Key Materials for Rechargeable Magnesium Batteries. *Adv. Energy Mater.* **11**, 2000787 (2021).
32. Guo, Z. *et al.* Recent Advances in Rechargeable Magnesium-Based Batteries for High-Efficiency Energy Storage. *Adv. Energy Mater.* **10**, 1903591 (2020).
33. Staiger, M. P., Pietak, A. M., Huadmai, J. & Dias, G. Magnesium and its alloys as orthopedic biomaterials: A review. *Biomaterials* **27**, 1728–1734 (2006).
34. Li, C.-S., Sun, Y., Gebert, F. & Chou, S.-L. Current Progress on Rechargeable Magnesium–Air Battery. *Adv. Energy Mater.* **7**, 1700869 (2017).
35. Zhou, J., Cheng, J., Wang, B., Peng, H. & Lu, J. Flexible metal–gas batteries: a potential option for next-generation power accessories for wearable electronics. *Energy Environ. Sci.* **13**, 1933–1970 (2020).
36. Snihirova, D. *et al.* Synergistic Mixture of Electrolyte Additives: A Route to a High-Efficiency Mg–Air Battery. *J. Phys. Chem. Lett.* **11**, 8790–8798 (2020).
37. Lee, D. U., Choi, J.-Y., Feng, K., Park, H. W. & Chen, Z. Advanced Extremely Durable 3D Bifunctional Air Electrodes for Rechargeable Zinc-Air Batteries. *Adv. Energy Mater.* **4**, 1301389 (2014).
38. Lima, F. H. B. *et al.* Catalytic Activity–d-Band Center Correlation for the O<sub>2</sub> Reduction Reaction on Platinum in Alkaline Solutions. *J. Phys. Chem. C* **111**, 404–410 (2007).
39. Zhang, J., Vukmirovic, M. B., Xu, Y., Mavrikakis, M. & Adzic, R. R. Controlling the Catalytic Activity of Platinum-Monolayer Electrocatalysts for Oxygen Reduction with Different Substrates. *Angew. Chem.* **117**, 2170–2173 (2005).
40. Janardhanan, V. M., Heuveline, V. & Deutschmann, O. Three-phase boundary length in solid-oxide fuel cells: A mathematical model. *J. Power Sources* **178**, 368–372 (2008).
41. Roussak, O. V. & Gesser, H. D. Electrochemistry, Batteries, and Fuel Cells. in *Applied Chemistry: A Textbook for Engineers and Technologists* (eds. Roussak, O. V. & Gesser, H. D.) 145–173 (Springer US, 2013). doi:10.1007/978-1-4614-4262-2\_9.
42. Cao, R., Lee, J.-S., Liu, M. & Cho, J. Recent Progress in Non-Precious Catalysts for Metal-Air Batteries. *Adv. Energy Mater.* **2**, 816–829 (2012).

43. Takeguchi, T. *et al.* Layered Perovskite Oxide: A Reversible Air Electrode for Oxygen Evolution/Reduction in Rechargeable Metal-Air Batteries. *J. Am. Chem. Soc.* **135**, 11125–11130 (2013).
44. Papas, E. B. & Sweeney, D. F. Interpreting the corneal response to oxygen: Is there a basis for re-evaluating data from gas-goggle studies? *Exp. Eye Res.* **151**, 222–226 (2016).
45. Neburchilov, V., Wang, H., Martin, J. J. & Qu, W. A review on air cathodes for zinc–air fuel cells. *J. Power Sources* **195**, 1271–1291 (2010).
46. Cheng, F. & Chen, J. Metal–air batteries: from oxygen reduction electrochemistry to cathode catalysts. *Chem. Soc. Rev.* **41**, 2172–2192 (2012).
47. Gewirth, A. A., Varnell, J. A. & DiAscro, A. M. Nonprecious Metal Catalysts for Oxygen Reduction in Heterogeneous Aqueous Systems. *Chem. Rev.* **118**, 2313–2339 (2018).
48. Al-Azawy, M. M. & Sari, F. Analysis of Dickson Voltage Multiplier for RF Energy Harvesting. in *2019 1st Global Power, Energy and Communication Conference (GPECOM)* 10–14 (2019). doi:10.1109/GPECOM.2019.8778492.
49. Kwon, K.-A. *et al.* High-speed camera characterization of voluntary eye blinking kinematics. *J. R. Soc. Interface* **10**, 20130227 (2013).
50. Fatt, I. & Weissman, B. A. *Physiology of the Eye: An Introduction to the Vegetative Functions.* (Butterworth-Heinemann, 2013).

## Figures

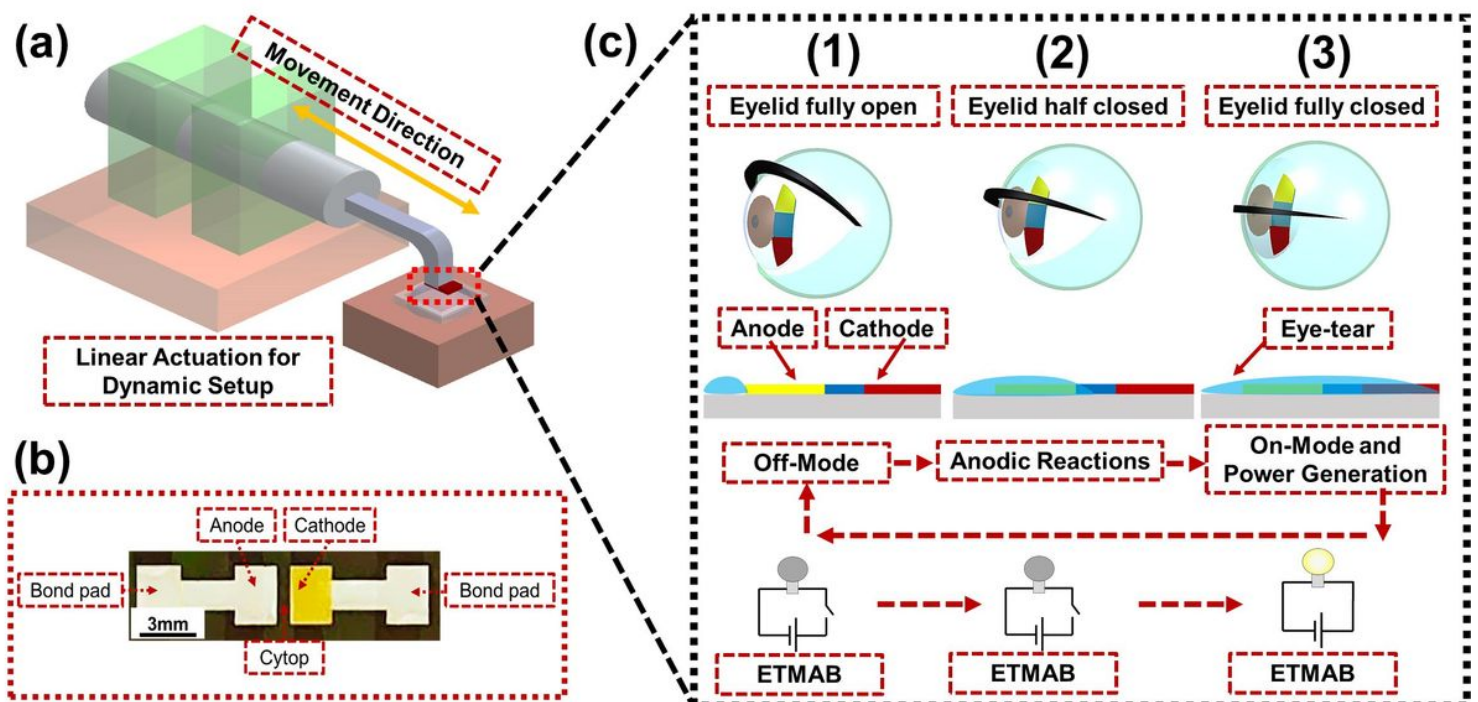


Figure 1

(a) Experimental setups, (b) device structure, and (c) working mechanism of the ETMAB.

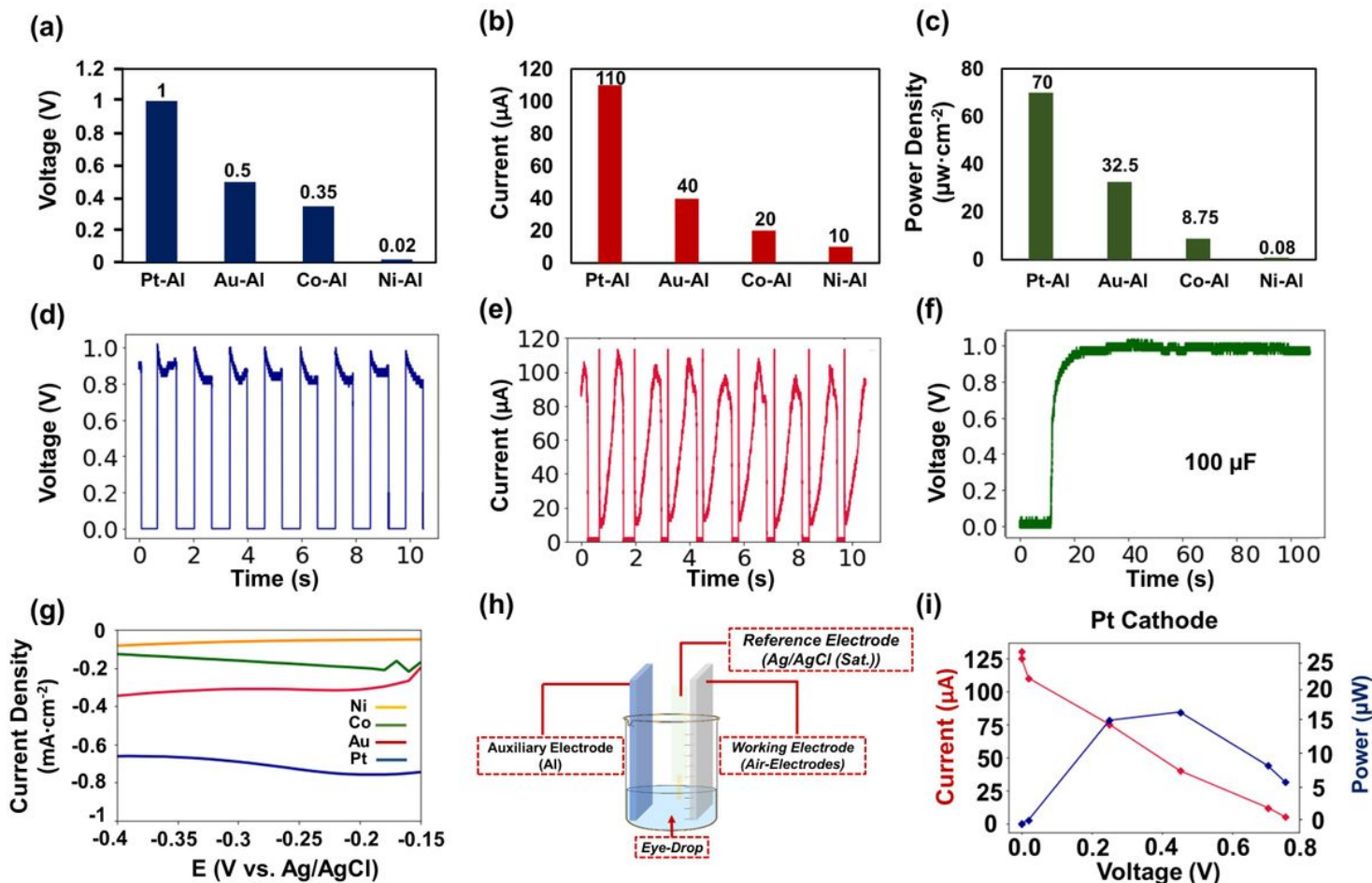


Figure 2

**Electrical outputs of the Al-air ETMAB while using different cathodes.** (a) Open circuit voltage of the Al-air ETMABs using different air-electrode cathodes, (b) maximum short-circuit current output of Al-air ETMABs using different air-electrodes, (c) impedance-matched load power-density of Al-air ETMABs using different air-electrodes, (d) voltage plot of the Al-air ETMAB using Pt as the air-electrode, (e) short circuit current plot of the Al-air ETMAB using Pt as the air-electrode, (f) charging curve of a 100  $\mu\text{F}$  capacitor using Al-air ETMAB with Pt cathode, (g) zoomed-in cyclic voltammetry test around the oxygen reduction potential for different air-electrodes including Ni, Co, Au, and Pt, (h) cyclic voltammetry set-up, and (i) load line and impedance matching analysis for Al-air ETMAB using Pt as the air-electrode.

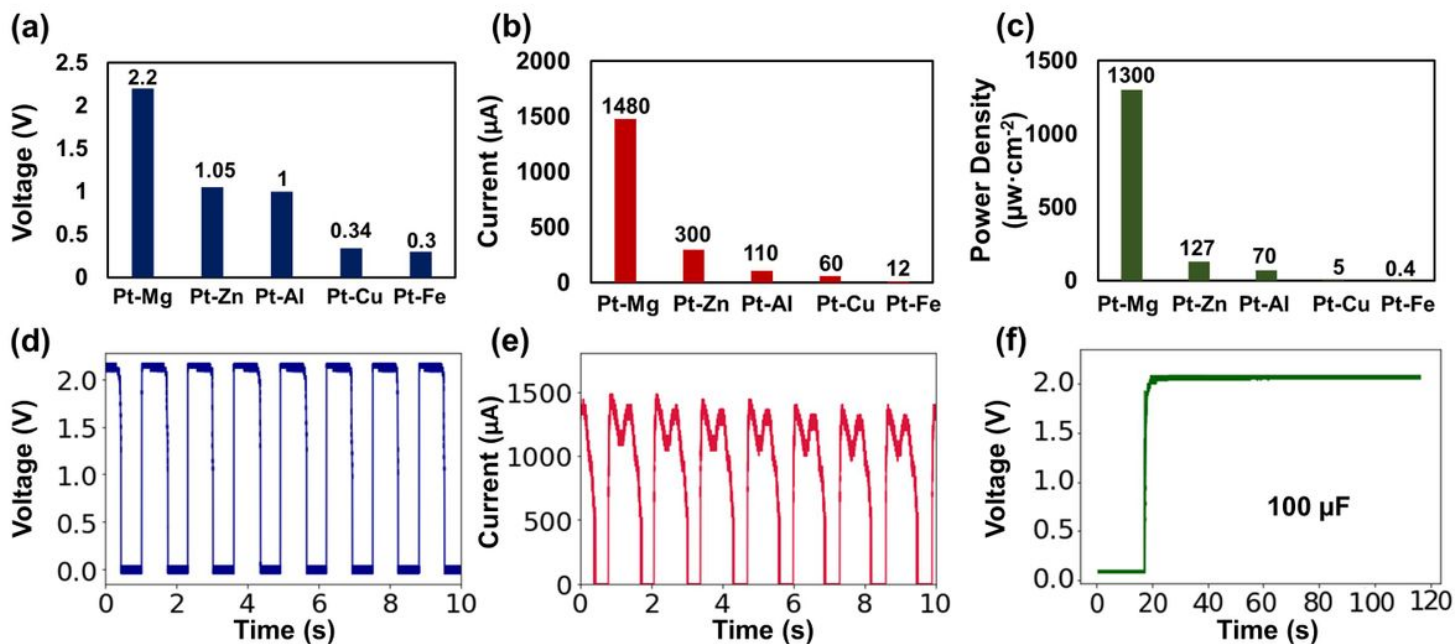


Figure 3

*Electrical outputs for the ETMABs using Pt cathode, moisturizing eye drop as the electrolyte, and different anode materials including Mg, Zn, Al, Cu, Fe; (a) open-circuit voltage of Pt cathode based ETMAB using different anodes, (b) maximum short circuit current of Pt cathode based ETMAB using different anodes, (c) impedance matched power density of Pt cathode based ETMAB using different anodes, (d) voltage output of Mg-air ETMAB, (e) short circuit current output of Mg-air ETMAB, and (f) charging curve of a 100  $\mu$ F capacitor using Mg-air ETMAB.*

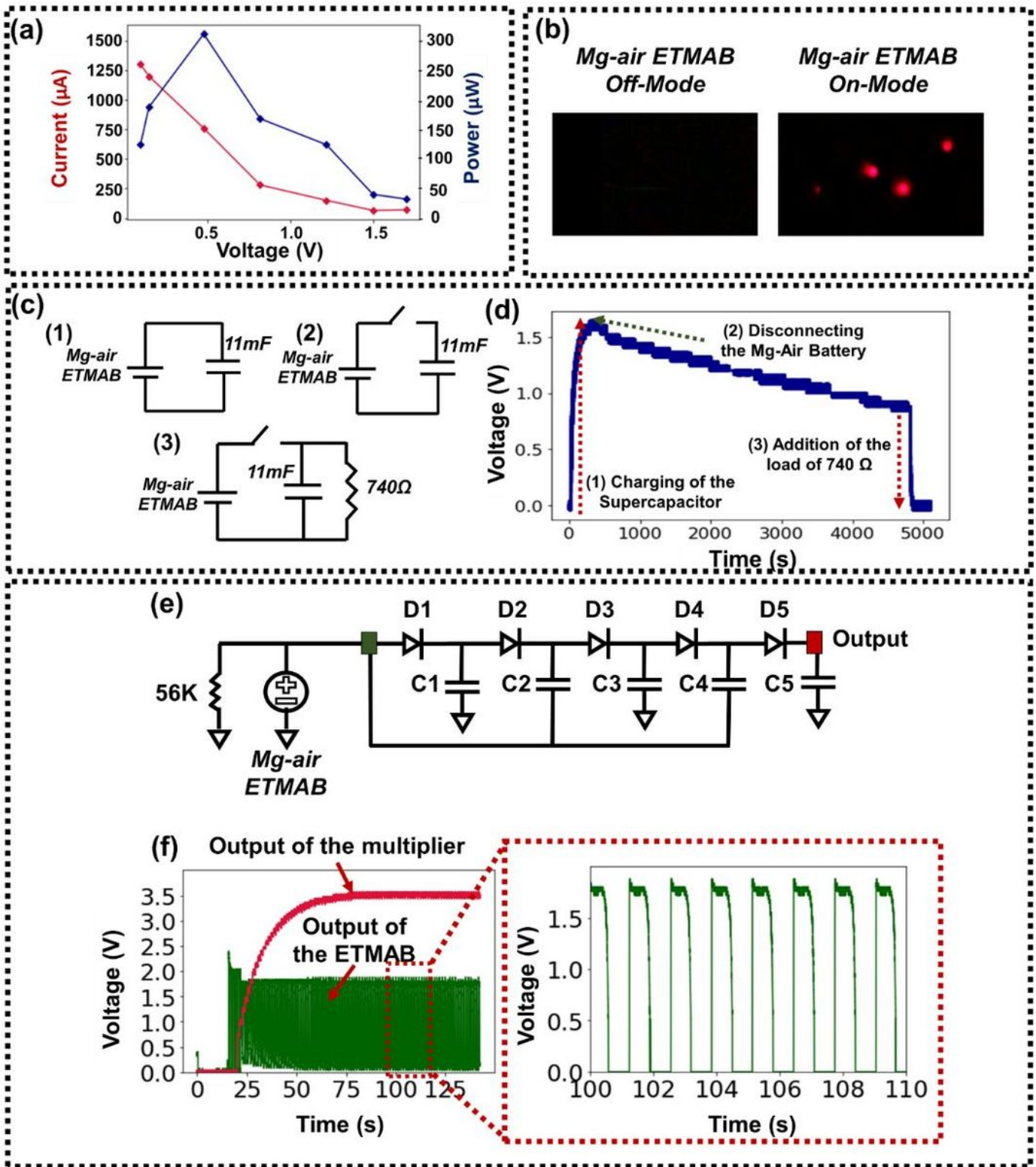


Figure 4

*Using Mg-air ETMAB for practical applications; (a) Impedance-matching and load line plots, (b) turning on four commercially available red LEDs, (c) circuit diagrams of three different stages of charging and discharging an 11 mF commercial super-capacitor, (d) charging and discharging curves of the 11 mF super-capacitor, (e) voltage-multiplier circuit, and (f) the outputs of the Mg-air ETMAB and the voltage-multiplier connected to the ETMAB while using a resistive load of 56 k $\Omega$ .*

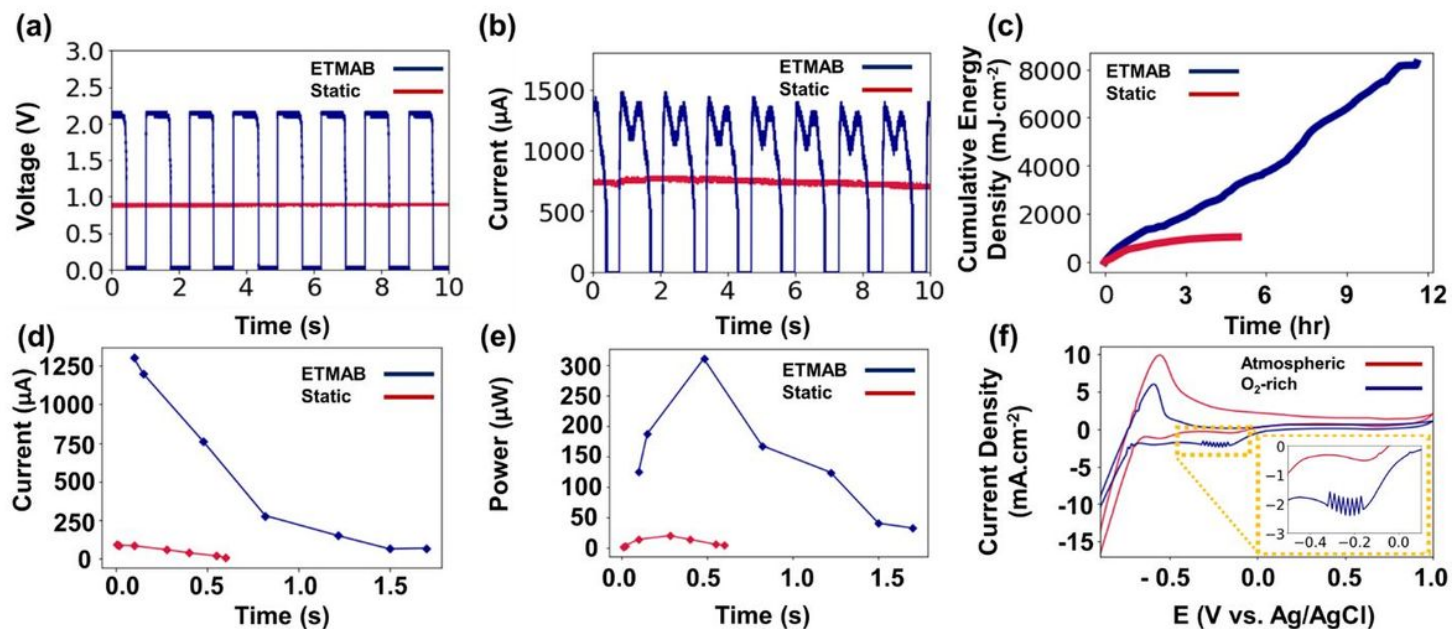


Figure 5

*The electrical properties of the stationary versus the motion-activated Mg-air batteries: (a) open-circuit voltage, (b) short-circuit current, (c) cumulative energy outputs under maximum power consuming load, (d) load lines, (e) power consumption curves, and (f) CV results showing the importance of  $O_2$  availability (inset shows the zoomed-in current density at the oxygen reduction potential with respect to the Ag/AgCl reference electrode).*

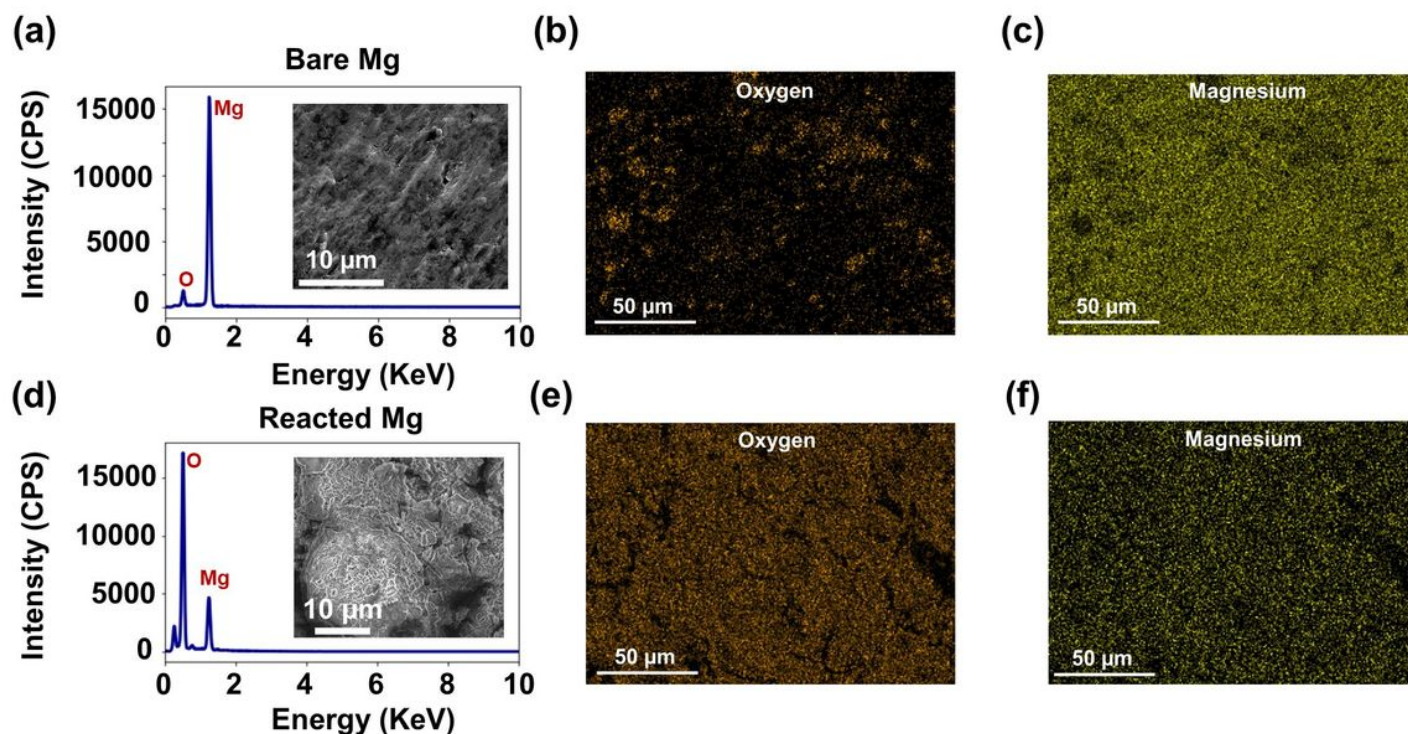
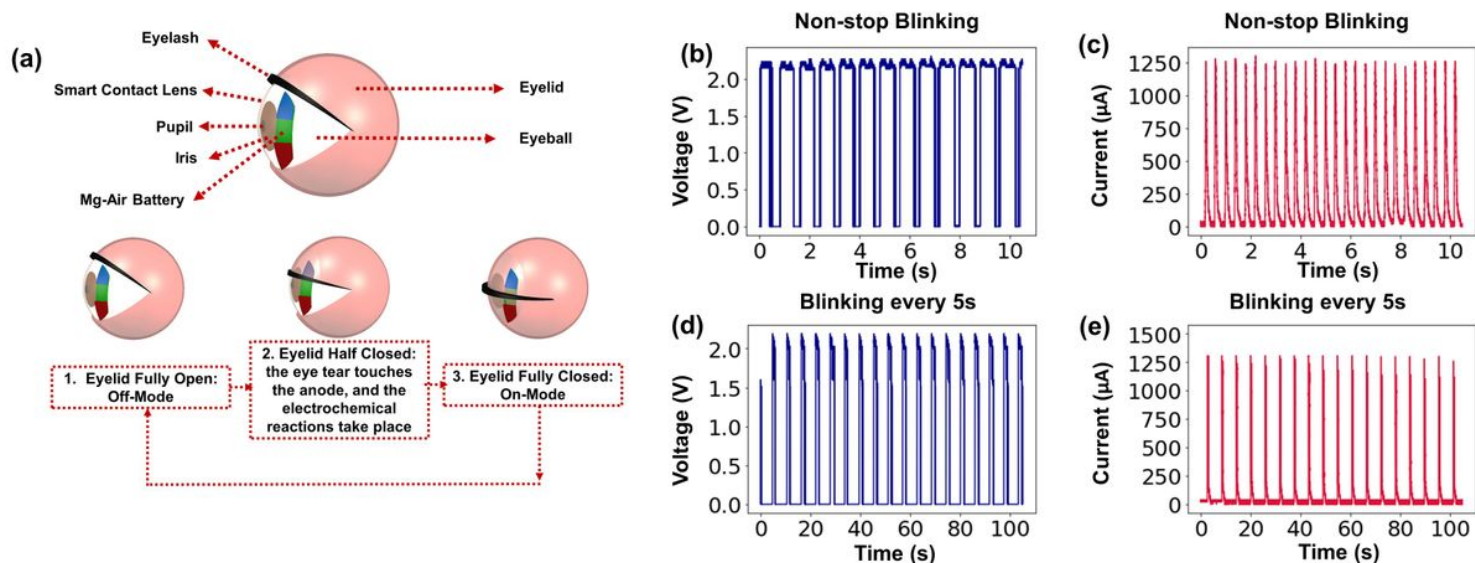


Figure 6

**Structural and morphological analysis of the Mg anode:** (a, b, and c) before and (d, e, and f) after electrochemical reactions.



**Figure 7**

(a) The working mechanism and (b, c, d, and e) the electrical outputs of the Mg-air ETMAB mounted on an eyeball replica.

## Supplementary Files

This is a list of supplementary files associated with this preprint. Click to download.

- [SupportingInformation.docx](#)
- [Video1MgairETMABlinearmotionLEDs.mp4](#)
- [Video2MgairETMABNonstoppeyblinkingmotion.mp4](#)